



HAL
open science

A spatially varying mathematical representation of the biventricular cardiac fiber architecture

Andreas Nagler, Cristóbal Bertoglio, Michael Ortiz, Wolfgang A. Wall

► **To cite this version:**

Andreas Nagler, Cristóbal Bertoglio, Michael Ortiz, Wolfgang A. Wall. A spatially varying mathematical representation of the biventricular cardiac fiber architecture. [Technical Report] Institute for Computational Mechanics, Technische Universität München; Center for Mathematical Modeling, Universidad de Chile 2016. hal-01280501

HAL Id: hal-01280501

<https://inria.hal.science/hal-01280501>

Submitted on 29 Feb 2016

HAL is a multi-disciplinary open access archive for the deposit and dissemination of scientific research documents, whether they are published or not. The documents may come from teaching and research institutions in France or abroad, or from public or private research centers.

L'archive ouverte pluridisciplinaire **HAL**, est destinée au dépôt et à la diffusion de documents scientifiques de niveau recherche, publiés ou non, émanant des établissements d'enseignement et de recherche français ou étrangers, des laboratoires publics ou privés.

A spatially varying mathematical representation of the biventricular cardiac fiber architecture

Andreas Nagler¹, Cristóbal Bertoglio², Michael Ortiz³, and Wolfgang A. Wall¹

¹Institute for Computational Mechanics, Technical University of Munich, Germany, {nagler,wall}@lnm.mw.tum.de

²Center for Mathematical Modeling, Universidad de Chile, Chile, cbertoglio@dim.uchile.cl

³Division of Engineering and Applied Science, California Institute of Technology, USA, ortiz@aero.caltech.edu

February 29, 2016

Abstract

We propose a framework for modeling complex, spatially varying fiber fields on arbitrary biventricular geometries. Using insights from histological observations we define the fiber direction in terms of a local reference system and two parametric fiber angle families on the epi- and endocardial surfaces. We then use classical harmonic extensions to interpolate the surface angle values to the whole volumetric, biventricular domain.

1 Introduction

It is widely accepted that cardiac cells have a preferred alignment direction, which is one of the main determinant of the electro-mechanical behavior of the heart. The complex pattern of ventricular fiber organization has been studied extensively in the last decades, see reviews [[Anderson et al., 2009](#), [Smerup et al., 2009](#)] and references therein.

In the case that noninvasive measurements are not available, simple mathematical descriptions of the fiber fields for simulations have been derived. These are translated from aforementioned experimental observations and are named rule-based models (RBM). Since RBM are based on the histological section of [[Streeter and Bassett, 1966](#), [Streeter et al., 1969](#)], they focus on the in-wall progression of the fibers, but do not consider any spatial variation in longitudinal (apex-to-base) and circumferential direction. Examples for RBMs differ

mainly in the way the given fiber directions on the epi- and endocardial surfaces are interpolated inwards the heart domain, either by using curvilinear coordinates [LeGrice et al., 1997, Rijcken et al., 1997], surface distance functions [Potse et al., 2006, Bishop et al., 2010] or harmonic liftings [Bayer et al., 2012, Wong and Kuhl, 2014, Rossi et al., 2014]. Hence, in this work we present a methodology that allows for surface variations of the fiber angles.

2 Methods

2.1 Fiber model assumptions

These are the main assumptions and justifications of our fiber model:

- 1: The fiber organization is modeled only at the macroscopic level as *single fiber continua* [Streeter and Hanna, 1973], where microscopic phenomena like branching and interdigitation are neglected.
- 2: The fiber direction is decomposed as proposed by [Streeter et al., 1969] into a local orthonormal reference system, namely *circumferential* \mathbf{c} , *longitudinal* \mathbf{l} and *radial* $\mathbf{r} = \mathbf{c} \times \mathbf{l}$ direction, and a set of two angles, namely the *helix angle* ϑ and the *transverse angle* φ . Though very often neglected in the RBM, the transverse angle is reported [Chen et al., 2005, Schmid et al., 2007] to have values up to 20° . Therefore both angles will be included into our model. A schematic description of the fiber orientation in context of the local reference system and the fiber angles is shown in Figure 1(a). The final equations for the fiber orientation then read

$$\mathbf{f} = \cos(\vartheta) \cos(\varphi) \mathbf{c} + \sin(\vartheta) \cos(\varphi) \mathbf{l} + \sin(\varphi) \mathbf{r} \quad (1)$$

- 3: The fiber orientation includes both a transmural (i.e. from epi- to endocardium, as identified in [Streeter et al., 1969]) and a longitudinal variation, based on the inspection of histological images in [Thomas, 1957, Fernandez-Teran and Hurle, 1982, Anderson et al., 2008] and fiber angle plots in [Ennis et al., 2008, Smerup et al., 2009, Lombaert et al., 2012].
- 4: Though reference [Fernandez-Teran and Hurle, 1982] reports three epicardial apexes, for the sake of simplicity the model is restricted to only one apex at the epicardium, where the *vortex cordis* \mathbf{a}_{epi} will originate. We also automatically define apical regions on the left and right endocardial surfaces as the closest points of these surfaces to \mathbf{a}_{epi} , what is needed for building the angle parametrization.

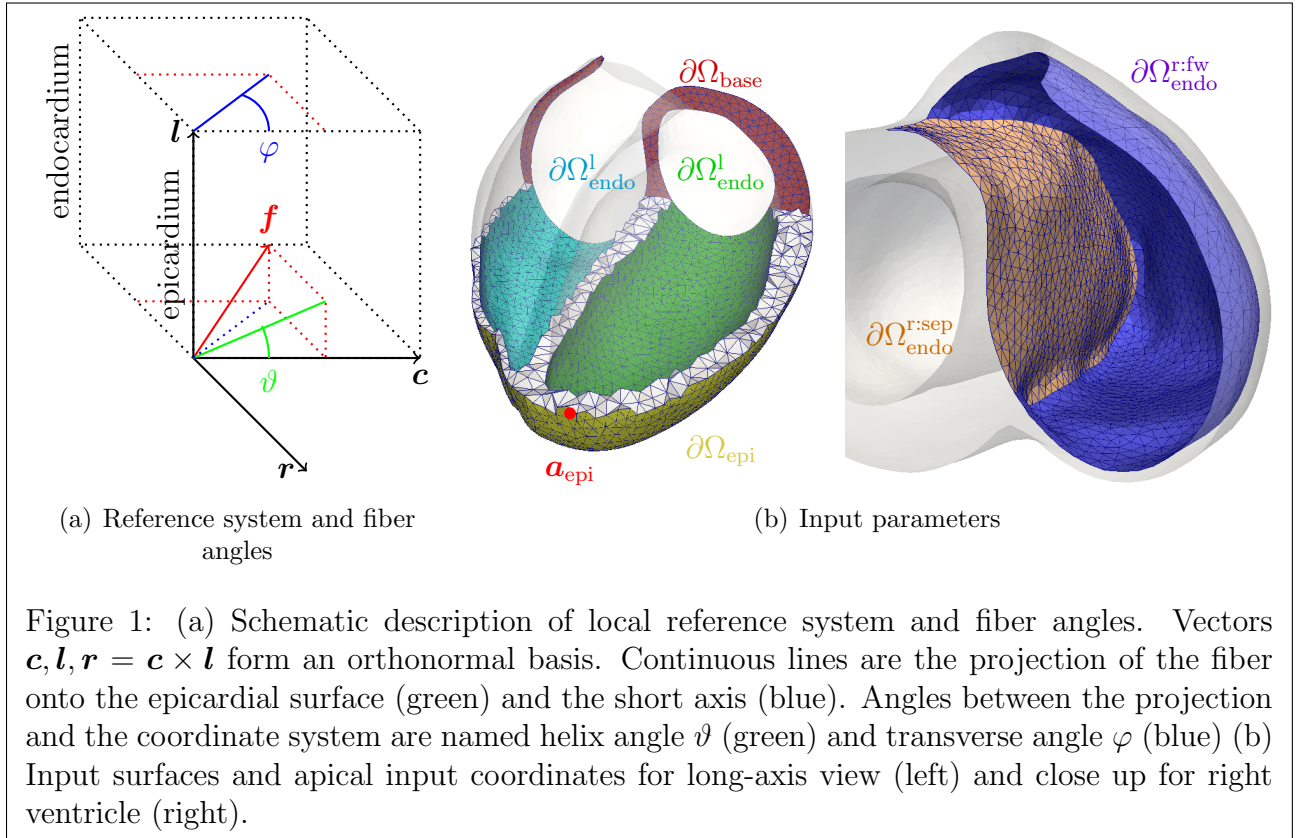
2.2 Basic input of RBM

The presented RBM needs the following input, which has to be provided by the user:

- Tessellation of the ventricular domain Ω , where the endocardial trabeculations are neglected, containing the mesh points $\{\mathbf{x}_1, \dots, \mathbf{x}_p\} \subset \Omega$.

- Subdivision of the ventricular surface $\partial\Omega$ into base $\partial\Omega_{\text{base}}$, epicardium $\partial\Omega_{\text{epi}}$, endocardium of the left and right ventricle $\partial\Omega_{\text{endo}}^l$ and $\partial\Omega_{\text{endo}}^r$, respectively. The latter is further subdivided into septal $\partial\Omega_{\text{endo}}^{r:\text{sep}}$ and the free wall $\partial\Omega_{\text{endo}}^{r:\text{fw}}$ regions. This can be integrated in the geometrical model construction typically done after the image segmentation.
- The epicardial apex coordinate \mathbf{a}_{epi} .
- The number of surface partitions for the angles parametrization. For the sake of generality, we will assume different number of patches for each surface of the heart $\Gamma \in \{\partial\Omega_{\text{epi}}, \partial\Omega_{\text{endo}}^l, \partial\Omega_{\text{endo}}^r\}$, which we will denote p_a^Γ and p_c^Γ for the axial and circumferential number of partitions, respectively. Note, however, that in the main part of the article we choose $p_a^\Gamma = p_c^\Gamma$.

A schematic overview of all input parameters are given in Figure 1(b).



2.3 Reference coordinate system

When all input surfaces and coordinates from Section 2.2 are given, the algorithm for computing a heart-adapted coordinate system reads:

C1: Set the long-axis directions \mathbf{l}_{epi} , $\mathbf{l}_{\text{endo}}^l$ and $\mathbf{l}_{\text{endo}}^r$ on each surface $\partial\Omega_{\text{epi}}$, $\partial\Omega_{\text{endo}}^l$ and $\partial\Omega_{\text{endo}}^r$, respectively. These directions are defined by computing the pseudo-normals of the nodes closest to \mathbf{a}_{epi} on each of the surfaces, see scheme in Figure 2(a).

C2: For each $\mathbf{x} \in \partial\Omega \setminus \partial\Omega_{\text{base}}$ compute the area-weighted nodal pseudo-normal $\tilde{\mathbf{n}}(\mathbf{x})$.

C3: For each $\mathbf{x} \in \partial\Omega \setminus \partial\Omega_{\text{base}}$ calculate the circumferential and longitudinal direction $\mathbf{c}_{2D}, \mathbf{l}_{2D} : \partial\Omega \setminus \partial\Omega_{\text{base}} \rightarrow [-1, 1]^3$ via:

$$\mathbf{c}_{2D}(\mathbf{x}) = \text{cross}(\lambda(\mathbf{x})\tilde{\mathbf{n}}(\mathbf{x}), \mathbf{l}(\mathbf{x})) \quad (2)$$

$$\mathbf{l}_{2D}(\mathbf{x}) = \text{cross}(\lambda(\mathbf{x})\tilde{\mathbf{n}}(\mathbf{x}), \mathbf{c}_{2D}(\mathbf{x})) \quad (3)$$

with

$$\lambda(\mathbf{x}) = \begin{cases} +1 & \text{for } \mathbf{x} \in \{\partial\Omega_{\text{epi}} \cup \partial\Omega_{\text{endo}}^{\text{r:sep}}\} \\ -1 & \text{for } \mathbf{x} \in \{\partial\Omega_{\text{epi}} \cup \partial\Omega_{\text{endo}}^{\text{r:sep}}\} \end{cases}, \quad \mathbf{l}(\mathbf{x}) = \begin{cases} \mathbf{l}_{\text{epi}} & \text{for } \mathbf{x} \in \partial\Omega_{\text{epi}} \\ \mathbf{l}_{\text{endo}}^l & \text{for } \mathbf{x} \in \partial\Omega_{\text{endo}}^l \\ \mathbf{l}_{\text{endo}}^r & \text{for } \mathbf{x} \in \partial\Omega_{\text{endo}}^r \end{cases} \quad (4)$$

This choice of λ assures that all normals point outwards the ventricular cavity. We hence implicitly fulfill the convention of [Streeter et al., 1969] that the circumferential direction points counterclockwise with respect to the apex-to-base view and the longitudinal direction points from apex to base. A schematic overview of \mathbf{c}_{2D} and \mathbf{l}_{2D} is shown in Figure 2(b).

C4: The quantities \mathbf{c}_{2D} and \mathbf{l}_{2D} are now extended to the whole ventricular domain versions $\mathbf{c}_{3D}, \mathbf{l}_{3D} : \Omega \rightarrow [-1, 1]^3$ by solving the following harmonic lifting:

$$\begin{aligned} \Delta \mathbf{c}_{3D} &= \mathbf{0} & \text{in } \Omega \\ \mathbf{c}_{3D} &= \mathbf{c}_{2D} & \text{on } \partial\Omega_{\text{epi}} \cup \partial\Omega_{\text{endo}}^l \cup \partial\Omega_{\text{endo}}^r \\ \partial_{\mathbf{n}_\Omega} \mathbf{c}_{3D} &= \mathbf{0} & \text{on } \partial\Omega_{\text{base}}, \end{aligned}$$

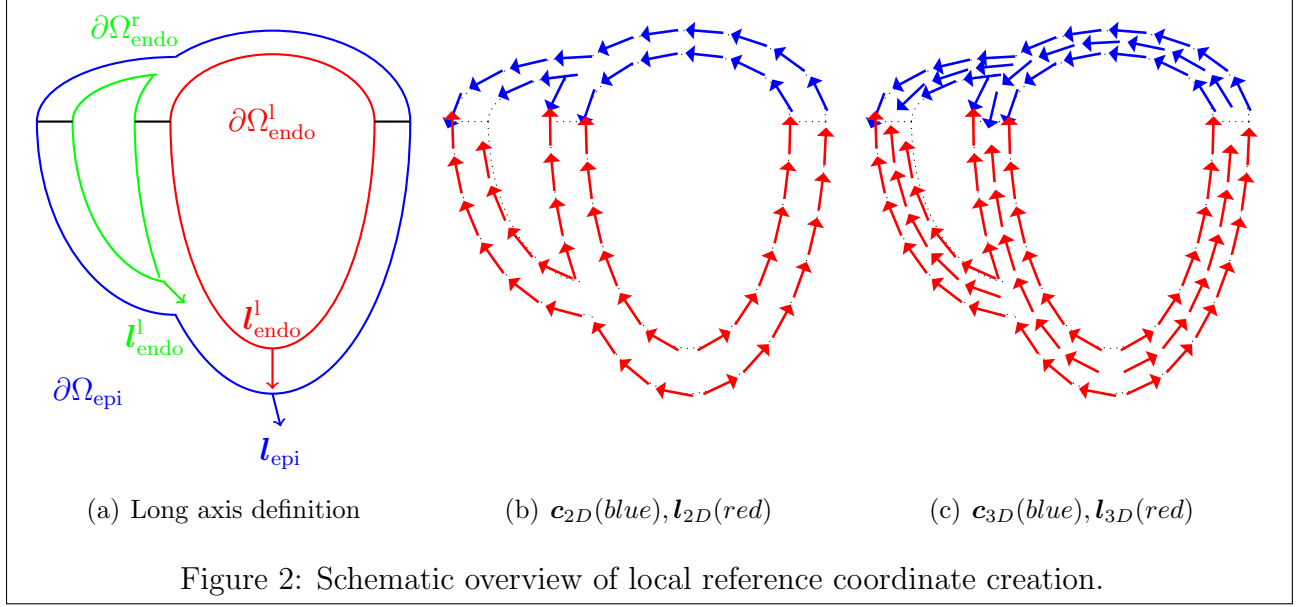
and analogously for \mathbf{l}_{3D} . Finally, both \mathbf{c}_{3D} and \mathbf{l}_{3D} are orthogonormalized at every mesh point.

The results of the single steps are depicted in Figure 2.

2.4 Ventricular manifold parametrization

An initial step in parametrizing the fiber angles is the computation of a two-dimensional manifold coordinate system for the ventricular surfaces $\partial\Omega_{\text{epi}}$, $\partial\Omega_{\text{endo}}^l$ and $\partial\Omega_{\text{endo}}^r$, see final results in Figure 3(c) and 3(f). The components of this coordinate system will be named *longitudinal* coordinate $\nu : \partial\Omega \rightarrow [0, 1]$ and *circumferential* coordinate $\xi : \partial\Omega \rightarrow [0, 1]$. The construction of the local reference system is adapted from [Bayer et al., 2012, Wong and Kuhl, 2014].

Be all input surfaces and coordinates from Section 2.2 given. For surface $\Gamma \in \{\partial\Omega_{\text{epi}}, \partial\Omega_{\text{endo}}^l, \partial\Omega_{\text{endo}}^r\}$ the algorithm then reads:



H1: Compute the auxiliary fields $\tilde{\nu}, \tilde{\xi} : \Omega \rightarrow [0, 1]$ by solving the following Poisson problems:

$\Delta \tilde{\nu} = 0 \quad \text{in } \Omega$ $\tilde{\nu} = 0 \quad \text{in } \mathbf{A}_0^\Gamma$ $\tilde{\nu} = 1 \quad \text{in } \mathbf{A}_1^\Gamma$ $\partial_{\mathbf{n}_\Omega} \tilde{\nu} = 0 \quad \text{in } \partial\Omega \setminus \{\mathbf{A}_0^\Gamma \cup \mathbf{A}_1^\Gamma\}$	$\Delta \tilde{\xi} = \mathbf{0} \quad \text{in } \Omega$ $\tilde{\xi} = 0 \quad \text{in } \mathbf{C}_0^\Gamma$ $\tilde{\xi} = 1 \quad \text{in } \mathbf{C}_1^\Gamma$ $\partial_{\mathbf{n}_\Omega} \tilde{\xi} = \mathbf{0} \quad \text{in } \partial\Omega \setminus \{\mathbf{C}_0^\Gamma \cup \mathbf{C}_1^\Gamma\}$
---	---

The Dirichlet surfaces are chosen as follows. For $\tilde{\nu}$, \mathbf{A}_0^Γ corresponds to the mesh point $\in \Gamma$ closest to the given coordinate \mathbf{a}_{epi} , and the surface \mathbf{A}_1^Γ is taken as $\partial\Omega_{\text{base}}$. For $\tilde{\xi}$, the surfaces $\mathbf{C}_0^\Gamma, \mathbf{C}_1^\Gamma$ are identified as the regions close to the four chamber plane but restricted to the free wall for both $\partial\Omega_{\text{epi}}$ and $\partial\Omega_{\text{endo}}^l$, and restricted to the septum for $\partial\Omega_{\text{endo}}^r$. The four chamber plane is automatically defined using the apex and the two valvular barycentric coordinates.

As an example, for the surface $\partial\Omega_{\text{epi}}$ the regions $\mathbf{A}_0^\Gamma, \mathbf{A}_1^\Gamma, \mathbf{C}_0^\Gamma, \mathbf{C}_1^\Gamma$ and the resulting $\tilde{\nu}$ and $\tilde{\xi}$ are depicted in Figures 3(a)-3(b) and 3(d)-3(e), respectively.

H2: Note that the Harmonic interpolation solutions $\tilde{\nu}$ and $\tilde{\xi}$ present a highly nonlinear transition between the zero and one Dirichlet conditions. In particular, the values for $\tilde{\nu}$ are mostly around one, i.e. the value imposed on the base. To provide a more homogeneous spatial distribution of the coordinate values, the ranking of positions encoded in $\tilde{\nu}$ and $\tilde{\xi}$ is used to define a transformed coordinate as follows. Two index sets \mathcal{I}_ν and \mathcal{I}_ξ are built via ranking the values of $\tilde{\nu}$ and $\tilde{\xi}$ for the nodes $\{\mathbf{x}_1, \dots, \mathbf{x}_m\} \subset \Gamma$, such that

$$\tilde{\nu}(\mathbf{x}_{\mathcal{I}_\nu(1)}) < \dots < \tilde{\nu}(\mathbf{x}_{\mathcal{I}_\nu(m)}), \quad \tilde{\xi}(\mathbf{x}_{\mathcal{I}_\xi(1)}) < \dots < \tilde{\xi}(\mathbf{x}_{\mathcal{I}_\xi(m)}) \quad (5)$$

From this sorting procedure we can define the transformations for the new coordinate distributions ν^Γ and ξ^Γ :

$$\nu^\Gamma(\mathbf{x}_{\mathcal{I}_\nu(j)}) = \frac{j}{m}, \quad \xi^\Gamma(\mathbf{x}_{\mathcal{I}_\xi(j)}) = \frac{j}{m}, \quad j = 1, \dots, m \quad (6)$$

The resulting coordinate distribution after the transformation is depicted in Figure 3(c) and 3(f).

The final coordinates ν and ξ then read

$$\nu(\mathbf{x}) = \begin{cases} \nu^{\partial\Omega_{\text{epi}}} & \text{for } \mathbf{x} \in \partial\Omega_{\text{epi}} \\ \nu^{\partial\Omega_{\text{endo}}^l} & \text{for } \mathbf{x} \in \partial\Omega_{\text{endo}}^l \\ \nu^{\partial\Omega_{\text{endo}}^r} & \text{for } \mathbf{x} \in \partial\Omega_{\text{endo}}^r \end{cases}, \quad \xi(\mathbf{x}) = \begin{cases} \xi^{\partial\Omega_{\text{epi}}} & \text{for } \mathbf{x} \in \partial\Omega_{\text{epi}} \\ \xi^{\partial\Omega_{\text{endo}}^l} & \text{for } \mathbf{x} \in \partial\Omega_{\text{endo}}^l \\ \xi^{\partial\Omega_{\text{endo}}^r} & \text{for } \mathbf{x} \in \partial\Omega_{\text{endo}}^r \end{cases} \quad (7)$$

2.5 Fiber angle parametrization

The derived manifold coordinate system $[\nu, \xi]$ is now used to introduce a parametric representation of the fiber angle fields $\vartheta, \varphi : [-90^\circ, 90^\circ] \rightarrow \Omega$. Denoting the given number of partitions p_c^Γ, p_a^Γ in circumferential and axial direction, respectively, for surfaces $\Gamma \in \{\partial\Omega_{\text{epi}}, \partial\Omega_{\text{endo}}^l, \partial\Omega_{\text{endo}}^r\}$, we proceed as follows:

Z1: The surface Γ will be evenly partitioned according to a given scalars p_a^Γ and p_c^Γ . The points affiliated to partition $\mathcal{P}_{j,k}^\Gamma$, $j = 1, \dots, p_a$, $k = 1, \dots, p_c$ are given by:

$$\mathcal{P}_{j,k}^\Gamma = \left\{ \mathbf{x} \in \Gamma \left| [\nu(\mathbf{x}), \xi(\mathbf{x})] \in \left[\frac{j-1}{p_a^\Gamma}, \frac{j}{p_a^\Gamma} \right] \times \left[\frac{k-1}{p_c^\Gamma}, \frac{k}{p_c^\Gamma} \right] \right. \right\} \quad (8)$$

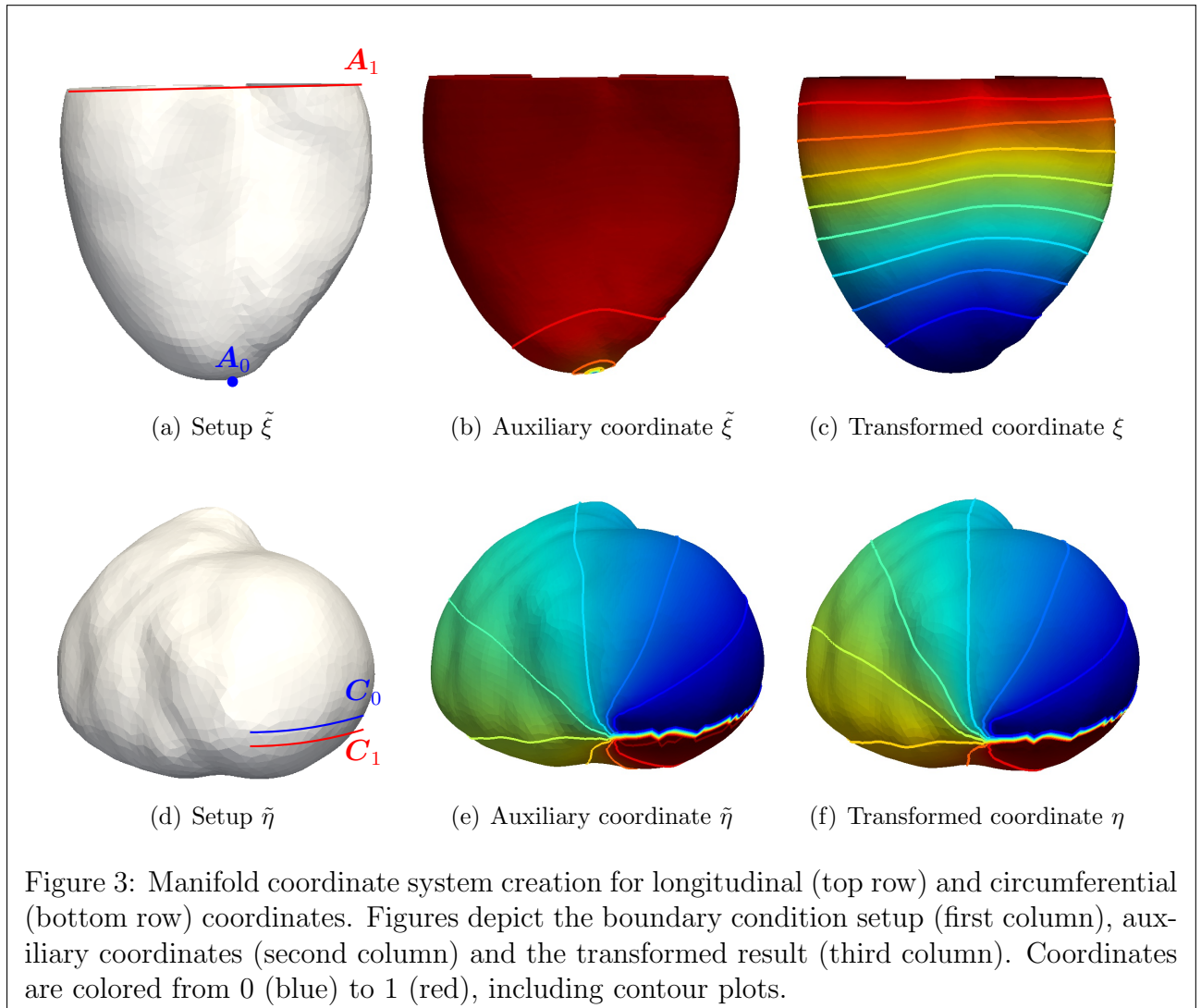
To preserve the continuity of each angle field near the apex, we define the partition \mathcal{P}_a^Γ , where we will apply a constant angle value. The region \mathcal{P}_a^Γ is constructed by merging the nodes with the smallest longitudinal coordinates of the partitions $\mathcal{P}_{0,k}^\Gamma$, $k = 1, \dots, p_c$ into \mathcal{P}_a^Γ , see Figure 4(a).

Z2: We introduce a set of degrees of freedom (DOF) $Z_{r,s}^\Gamma$, $r = 0, \dots, p_a^\Gamma$, $s = 0, \dots, p_c^\Gamma$, representing the values for either the transverse or helix angle on the corners of the partitions defined above, see Figure 4(a). These will be later interpolated to the rest of the heart domain to construct the respective full 3D angle field.

First, note that due to introduction of the apical partition \mathcal{P}_a^Γ , we impose the following constraint

$$Z_{0,1}^\Gamma = \dots = Z_{0,p_c}^\Gamma \stackrel{\text{def}}{=} Z_a^\Gamma \quad (9)$$

and we also set Z_a^Γ as the angle value on \mathcal{P}_a^Γ .



Additionally, for each Γ the first and last partitions in circumferential direction are connected, namely $\mathcal{P}_{j,1}^\Gamma$ and $\mathcal{P}_{j,p_c}^\Gamma$. Therefore the following DOFs have to be enforced to be equal:

$$Z_{j,0}^\Gamma = Z_{j,p_c}^\Gamma, \quad j = 0, \dots, p_a^\Gamma. \quad (10)$$

Both constraints lead to the final set of angle DOFs \mathbf{Z}^Γ with the effective size $\kappa^\Gamma = 1 + p_a^\Gamma p_c^\Gamma$.

Z3: We define now the function $z_{2D}^\Gamma : \mathbb{R}^{\kappa^\Gamma} \times \Gamma \rightarrow \mathbb{R}$ representing the piecewise linear interpolation of the DOFs to the rest of the surface Γ . For the interpolation scheme the partition is divided into the two triangles \mathbf{T}_1 and \mathbf{T}_2 , where a classical isoparametric interpolation concept is used. Therefore the interpolation reads

$$z_{2D}^\Gamma(\mathbf{Z}^\Gamma, \mathbf{x}) = \begin{cases} r_1(\mathbf{x})Z_{j-1,k-1}^\Gamma + (1 - r_1(\mathbf{x}) - s_1(\mathbf{x}))Z_{j,k-1}^\Gamma + s_1(\mathbf{x})Z_{j,k}^\Gamma & \text{for } \mathbf{x} \in \mathbf{T}_1 \\ r_2(\mathbf{x})Z_{j-1,k-1}^\Gamma + s_2(\mathbf{x})Z_{j,k}^\Gamma + (1 - r_2(\mathbf{x}) - s_2(\mathbf{x}))Z_{j-1,k}^\Gamma & \text{for } \mathbf{x} \in \mathbf{T}_2 \end{cases}$$

where the local triangle coordinates $[r_1(\mathbf{x}), s_1(\mathbf{x})]$ and $[r_2(\mathbf{x}), s_2(\mathbf{x})]$, respectively, are computed by solving the the following systems of equations for each \mathbf{x} :

$$\begin{bmatrix} \nu(\mathbf{x}) \\ \xi(\mathbf{x}) \end{bmatrix} = r_1(\mathbf{x}) \begin{bmatrix} \frac{j-1}{p_a} \\ \frac{k-1}{p_c} \end{bmatrix} + s_1(\mathbf{x}) \begin{bmatrix} \frac{j}{p_a} \\ \frac{k-1}{p_c} \end{bmatrix} + (1 - r_1(\mathbf{x}) - s_1(\mathbf{x})) \begin{bmatrix} \frac{j}{p_a} \\ \frac{k}{p_c} \end{bmatrix} \text{ for } \mathbf{x} \in \mathbf{T}_1 \quad (11)$$

$$\begin{bmatrix} \nu(\mathbf{x}) \\ \xi(\mathbf{x}) \end{bmatrix} = r_2(\mathbf{x}) \begin{bmatrix} \frac{j-1}{p_a} \\ \frac{k-1}{p_c} \end{bmatrix} + s_2(\mathbf{x}) \begin{bmatrix} \frac{j}{p_a} \\ \frac{k}{p_c} \end{bmatrix} + (1 - r_2(\mathbf{x}) - s_2(\mathbf{x})) \begin{bmatrix} \frac{j-1}{p_a} \\ \frac{k}{p_c} \end{bmatrix} \text{ for } \mathbf{x} \in \mathbf{T}_2 \quad (12)$$

The interpolation scheme including the triangles and the definition of r_1, s_1, r_2, s_2 is exemplified for one partition in Figure 4(b).

Using the definition $\mathbf{Z} \stackrel{\text{def}}{=} [\mathbf{Z}^{\partial\Omega_{\text{epi}}}, \mathbf{Z}^{\partial\Omega_{\text{endo}}^1}, \mathbf{Z}^{\partial\Omega_{\text{endo}}^r}]$ with size $\kappa^{\partial\Omega} = \kappa^{\partial\Omega_{\text{epi}}} + \kappa^{\partial\Omega_{\text{endo}}^1} + \kappa^{\partial\Omega_{\text{endo}}^r}$ the final scalar function $z_{3D} : \mathbb{R}^{\kappa^{\partial\Omega}} \times \Omega \rightarrow \mathbb{R}$ is now computed by solving the following harmonic interpolation:

$$\Delta z_{3D}(\mathbf{Z}, \mathbf{x}) = 0 \quad \text{in } \Omega \quad (13)$$

$$z_{3D}(\mathbf{Z}, \mathbf{x}) = z_{2D}^{\partial\Omega_{\text{epi}}}(\mathbf{Z}^{\partial\Omega_{\text{epi}}}, \mathbf{x}) \quad \text{on } \partial\Omega_{\text{epi}} \quad (14)$$

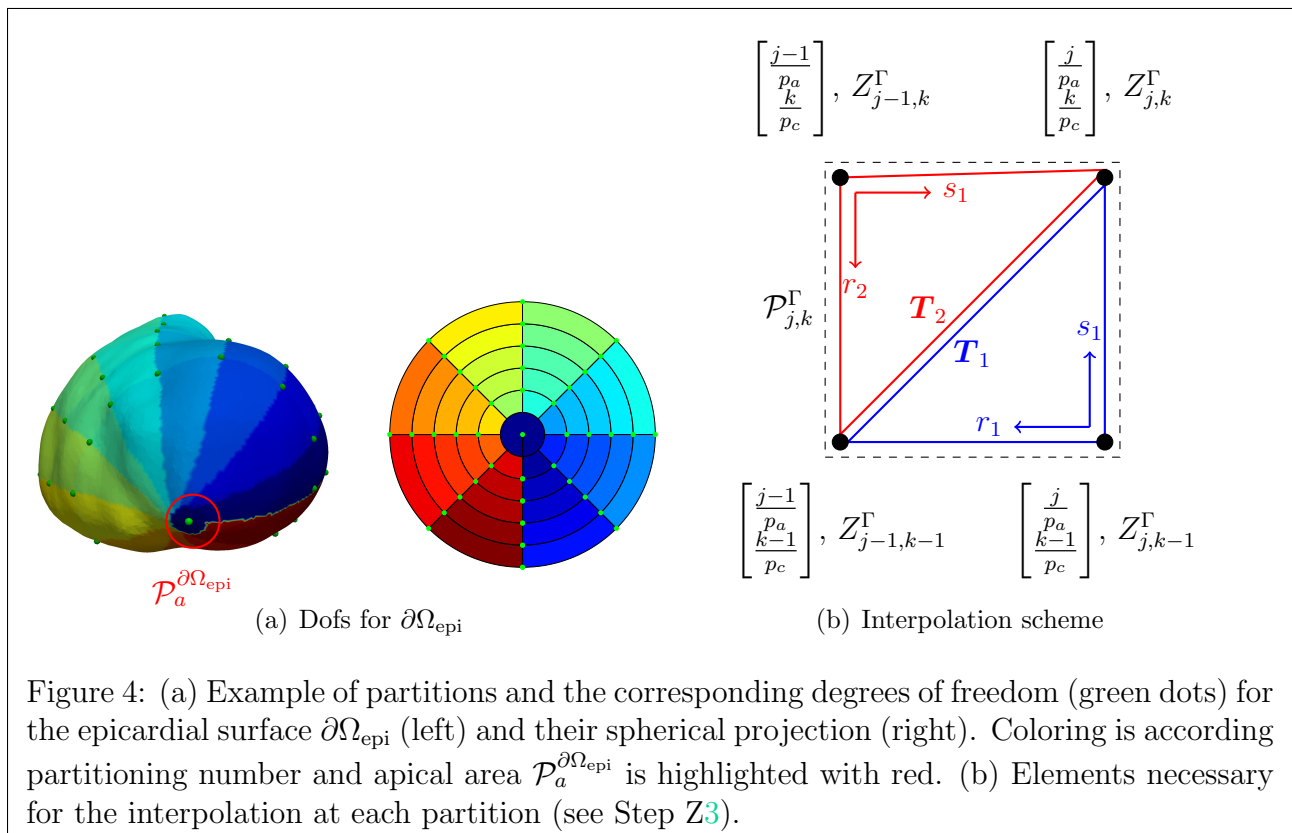
$$z_{3D}(\mathbf{Z}, \mathbf{x}) = z_{2D}^{\partial\Omega_{\text{endo}}^1}(\mathbf{Z}^{\partial\Omega_{\text{endo}}^1}, \mathbf{x}) \quad \text{on } \partial\Omega_{\text{endo}}^1 \quad (15)$$

$$z_{3D}(\mathbf{Z}, \mathbf{x}) = z_{2D}^{\partial\Omega_{\text{endo}}^r}(\mathbf{Z}^{\partial\Omega_{\text{endo}}^r}, \mathbf{x}) \quad \text{on } \partial\Omega_{\text{endo}}^r \quad (16)$$

$$\partial_{\mathbf{n}_\Omega} z_{3D}(\mathbf{Z}, \mathbf{x}) = 0 \quad \text{on } \partial\Omega_{\text{base}} \quad (17)$$

Note that procedure Z1-Z3 involves only linear operations for computing the field z_{3D} from the DOFs \mathbf{Z} , which can be summarized as

$$z_{3D}(\mathbf{Z}, \mathbf{x}_j) = \mathcal{Z}_j \mathbf{Z} \quad (18)$$



with \mathcal{Z}_j the j -th line of the linear operator \mathcal{Z} . Notice that the i -th column of \mathcal{Z} hence corresponds to solving the steps **Z1-Z3** with \mathcal{Z} equaling the i -th unitary vector. Therefore, \mathcal{Z} can be pre-computed independently of the specific values for the angle dofs \mathcal{Z} that may be later assigned.

References

- [Anderson et al., 2008] Anderson, R. H., Sanchez-Quintana, D., Niederer, P., and Lunkenheimer, P. P. (2008). Structural–functional correlates of the 3-dimensional arrangement of the myocytes making up the ventricular walls. *J. Thorac. Cardiovasc. Surg.*, 136(1):10–18.
- [Anderson et al., 2009] Anderson, R. H., Smerup, M., Sanchez-Quintana, D., Loukas, M., and Lunkenheimer, P. P. (2009). The three-dimensional arrangement of the myocytes in the ventricular walls. *Clic. Anat.*, 22(1):64–76.
- [Bayer et al., 2012] Bayer, J., Blake, R., Plank, G., and Trayanova, N. (2012). A novel rule-based algorithm for assigning myocardial fiber orientation to computational heart models. *Ann. Biomed. Eng.*, 40:2243–2254.
- [Bishop et al., 2010] Bishop, M. J., Plank, G., Burton, R. A. B., Schneider, J. E., Gavaghan, D. J., Grau, V., and Kohl, P. (February 2010). Development of an anatomically detailed MRI-derived rabbit ventricular model and assessment of its impact on simulations of electrophysiological function. *Am. J. Physiol.*, 298(2):H699–H718.
- [Chen et al., 2005] Chen, J., Liu, W., Zhang, H., Lacy, L., Yang, X., Song, S.-K., Wickline, S. A., and Yu, X. (2005). Regional ventricular wall thickening reflects changes in cardiac fiber and sheet structure during contraction: quantification with diffusion tensor MRI. *Am. J. Physiol.*, 289(5):H1898–H1907.
- [Ennis et al., 2008] Ennis, D. B., Nguyen, T. C., Riboh, J. C., Wigström, L., Harrington, K. B., Daughters, G. T., Ingels, N. B., and Miller, D. C. (2008). Myofiber angle distributions in the ovine left ventricle do not conform to computationally optimized predictions. *J. Biomech.*, 41(15):3219–3224.
- [Fernandez-Teran and Hurle, 1982] Fernandez-Teran, M. and Hurle, J. (1982). Myocardial fiber architecture of the human heart ventricles. *Anat. Rec.*, 204(2):137–147.
- [LeGrice et al., 1997] LeGrice, I. J., Hunter, P. J., , and Smaill, B. H. (1997). Laminar structure of the heart: a mathematical model. *Am. Physiol. Soc.*, 272:H2466–H2476.
- [Lombaert et al., 2012] Lombaert, H., Peyrat, J., Croisille, P., Rapacchi, S., Fanton, L., Cheriet, F., Clarysse, P., Magnin, I., Delingette, H., and Ayache, N. (2012). Human atlas of the cardiac fiber architecture: study on a healthy population. *IEEE Trans. Med. Imag.*, 31(7):1436–1447.

- [Potse et al., 2006] Potse, M., Dube, B., Richer, J., Vinet, A., and Gulrajani, R. (2006). A comparison of monodomain and bidomain reaction-diffusion models for action potential propagation in the human heart. IEEE Trans. Biomed. Eng., 53:2425–2435.
- [Rijcken et al., 1997] Rijcken, J., Bovendeerd, P. H., Schoofs, A. J., van Campen, D. H., and Arts, T. (1997). Optimization of cardiac fiber orientation for homogeneous fiber strain at beginning of ejection. J. Biomech., 30(10):1041–1049.
- [Rossi et al., 2014] Rossi, S., Lassila, T., Ruiz-Baier, R., Sequeira, A., and Quarteroni, A. (2014). Thermodynamically consistent orthotropic activation model capturing ventricular systolic wall thickening in cardiac electromechanics. Eur. J. Mech. - A/Solids, 48(0):129 – 142.
- [Schmid et al., 2007] Schmid, P., Lunkenheimer, P. P., Redmann, K., Rothaus, K., Jiang, X., Cryer, C. W., Jaermann, T., Niederer, P., Boesiger, P., and Anderson, R. H. (2007). Statistical analysis of the angle of intrusion of porcine ventricular myocytes from epicardium to endocardium using diffusion tensor magnetic resonance imaging. Anat. Rec., 290(11):1413–1423.
- [Smerup et al., 2009] Smerup, M., Nielsen, E., Agger, P., Frandsen, J., Vestergaard-Poulsen, P., Andersen, J., Nyengaard, J., Pedersen, M., Ringgaard, S., Hjortdal, V., et al. (2009). The three-dimensional arrangement of the myocytes aggregated together within the mammalian ventricular myocardium. Anat. Rec., 292(1):1–11.
- [Streeter and Bassett, 1966] Streeter, D. D. and Bassett, D. L. (1966). An engineering analysis of myocardial fiber orientation in pig’s left ventricle in systole. Anat. Rec., 155(4):503–511.
- [Streeter and Hanna, 1973] Streeter, D. D. and Hanna, W. T. (1973). Engineering mechanics for successive states in canine left ventricular myocardium: II. fiber angle and sarcomere length. Circ. Res., 33(6):656–664.
- [Streeter et al., 1969] Streeter, D. D., Spotnitz, H. M., Patel, D. P., Ross, J., and Sonnenblick, E. H. (1969). Fiber orientation in the canine left ventricle during diastole and systole. Circ. Res., 24(3):339–347.
- [Thomas, 1957] Thomas, C. E. (1957). The muscular architecture of the ventricles of hog and dog hearts. Am. J. Anat., 101(1):17–57.
- [Wong and Kuhl, 2014] Wong, J. and Kuhl, E. (2014). Generating fibre orientation maps in human heart models using poisson interpolation. Comput. Methods Biomech. Biomed. Eng., 17(11):1217–1226.